Supplementary materials for "Unusual Diffusion of Chiral Active Brownian Particles in Deformable and Displaceable Media"

Kexin Zhang,[1] Yuxin Tian,[1] Xiaoting Yu,[1] Hongwei Zhu,[2] Yanwei Li,[1] Mingcheng Yang,[3,4,*] Peng Liu,[1,†] Ning Zheng,[1,‡] and Luhui Ning[5,6,§]

[1] *School of Physics, Beijing Institute of Technology, Beijing 100081, China*

[2] *School of Physical Science and Technology, Key Laboratory of Magnetism and Magnetic Materials for Higher Education in Inner Mongolia Autonomous Region, Baotou Teachers' College, Baotou 014030, China*

[3] *Beijing National Laboratory for Condensed Matter Physics and Laboratory of Soft Matter Physics, Institute of Physics, Chinese Academy of Sciences, Beijing 100190, China*

[4] *School of Physical Sciences, University of Chinese Academy of Sciences, Beijing 100049, China*

[5] *Beijing Key Laboratory of Optical Detection Technology for Oil and Gas, China University of Petroleum-Beijing, Beijing 102249, China*

[6] *Basic Research Center for Energy Interdisciplinary, College of Science, China University of Petroleum-Beijing, Beijing 102249, China*

* mcyang@iphy.ac.cn

† liupeng@bit.edu.cn

‡ ningzheng@bit.edu.cn

§ lhningphy@cup.edu.cn

SUPPLEMENTARY NOTE 1: ROBUSTNESS OF NONMONOTONIC DIFFUSION WITH DIFFERENT OBSTACLE SIZES

To directly address the relative length scales of the Hexbugs and obstacles, additional experiments were performed in which the obstacle diameter varied to 1.5σ and $2\sigma/3$, with the original size of obstacle diameter $\sigma = 4.90$ cm, while keeping the CABP orbital radius fixed at $r = 3.76$ cm. As shown in Fig. S1, the normalized diffusion coefficient D/D_0 consistently exhibits a pronounced nonmonotonic dependence on the obstacle area fraction ϕ for all obstacle sizes tested, which only slightly influence the magnitude of diffusion coefficient D/D_0 and the diffusion maximum consistently occurs at $\phi_c = 0.70$. These results demonstrate that the observed nonmonotonic diffusion behavior is robust features of the system, governed primarily by the competition between obstacle-induced motion collimation and the suppression of CABP migration velocity rather than the specific geometric length ratio.

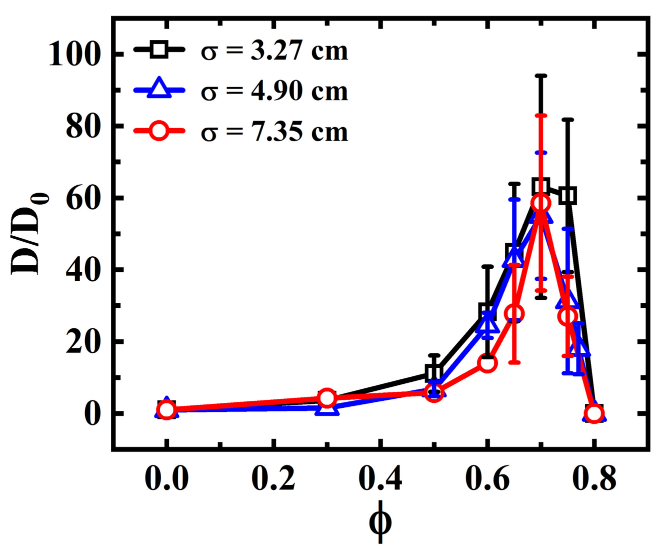

FIG. S1. Effect of obstacle size on the diffusion. Normalized diffusion coefficient of CABPs with $r = 3.76$ cm as a function of obstacle area fraction for different obstacle diameter. Error bars represent the standard deviation calculated over 3 independent measurements and are not visible when smaller than the symbol size.

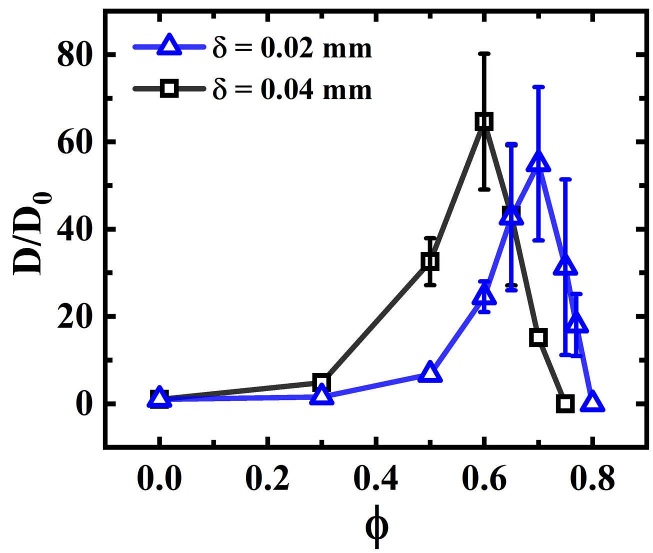

FIG. S2. Effect of obstacle softness on the diffusion. Normalized diffusion coefficient versus obstacle area fraction for a CABP with $r = 3.76$ cm, obtained with ring obstacles of thickness $\delta = 0.02$ mm (blue) and 0.04 mm (black). Error bars represent the standard deviation calculated over 3 independent measurements and are not visible when smaller than the symbol size.

SUPPLEMENTARY NOTE 2: EFFECT OF OBSTACLE SOFTNESS ON THE DIFFUSION OF CABPS

To evaluate the role of obstacle softness on the diffusion of CABPs, we performed comparative experiments using soft ring obstacles with a thickness of 0.02 mm thick and more rigid ring obstacles with a thickness of 0.04 mm, while keeping the CABP orbital radius fixed at $r = 3.76$ cm. The results, presented in Fig. S2, show that the qualitative nonmonotonic dependence of D/D_0 on the area fraction ϕ is preserved with rigid obstacles, indicating that the emergence of diffusion enhancement at intermediate crowding does not exclusively depend on obstacle softness alone. Quantitatively, however, the diffusion maximum occurs at a smaller critical area fraction ϕ_c for the more rigid rings, which can be attributed to their reduced deformability of rigid obstacles. Rigid obstacles resist deformation and displacement more strongly, leading to more effective collisions and an earlier suppression of translational motion as ϕ. Consequently, the balance between obstacle-induced motion collimation and velocity suppression is reached at lower obstacle density. These findings indicate that while the nonmonotonic diffusion originates from a generic competition between motion collimation and migration suppression in displaceable media, obstacle softness modulates the transport efficiency and the location of the diffusion maximum. This sensitivity highlights the relevance of soft and deformable obstacles for modeling active transport in biologically relevant settings, where environmental structures are typically soft rather than rigid.

SUPPLEMENTARY NOTE 3: INFLUENCE OF CONFINEMENT GEOMETRY ON CABP DIFFUSION

To investigate the potential influence of confinement geometry, We performed additional control experiments in a simple confinement with $R_{in} = 0$ cm, where CABPs move within a fully circular domain. The nonmonotonic dependence of the normalized diffusion coefficient D/D_0 on the area fraction ϕ still persists [Fig. S3], in qualitative agreement with the behavior observed in the annular geometry. This result demonstrates that the nonmonotonic diffusion enhancement is not specific to the annular confinement, but instead arises from the CABP-obstacle interactions.

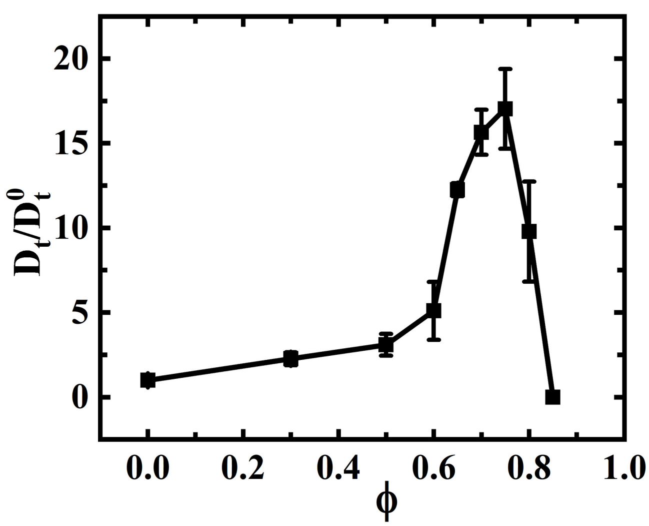

FIG. S3. Diffusion of chiral active Brownian particle. Normalized diffusion coefficient for CABP with $r = 3.76$ cm as a function of ϕ without inner boundary. Error bars represent the standard deviation calculated over 3 independent measurements and are not visible when smaller than the symbol size.

We also performed additional experiments with a reduced inner boundary, setting $R_{in} = 3.76$ cm to match the orbital radius of a representative CABP. As shown in Fig. S4, the

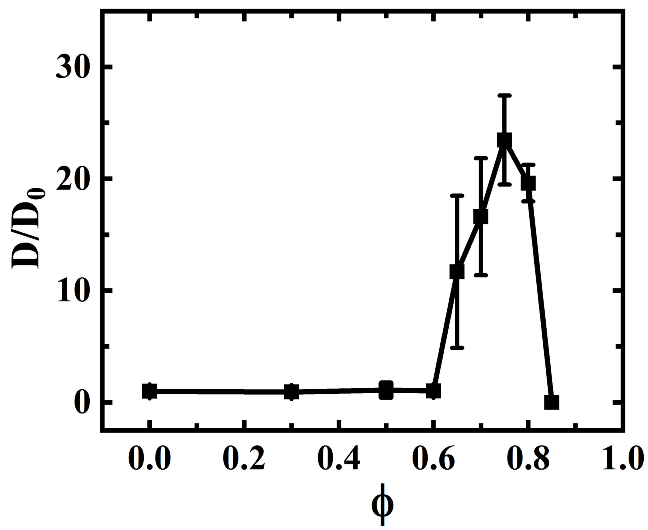

FIG. S4. Diffusion of chiral active Brownian particle. Normalized diffusion coefficient as a function of ϕ for CABP with $r = 3.76$ cm, measured in an annular confinement with inner boundary radius $R_{in} = 3.76$ cm. Error bars represent the standard deviation calculated over 3 independent measurements and are not visible when smaller than the symbol size.

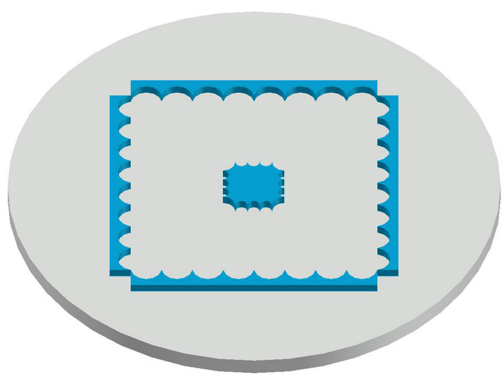

FIG. S5. Experimental setup with square-shaped confinement boundaries.

normalized diffusion coefficient D/D_0 continues to exhibit a pronounced nonmonotonic dependence on the obstacle area fraction ϕ, without any additional enhancement relative to the original annular geometry. This result indicates that no special transport enhancement emerges from the condition $r = R_{in}$, and the observed nonmonotonic diffusion behavior remains a robust consequence of CABP-obstacle interactions, rather than an effect arising from the specific choice of confinement geometry.

The diffusion behavior of CABP was further examined in a square-shaped confinement with an outer boundary of 70 cm and an inner boundary of 14.5 cm, while keeping the

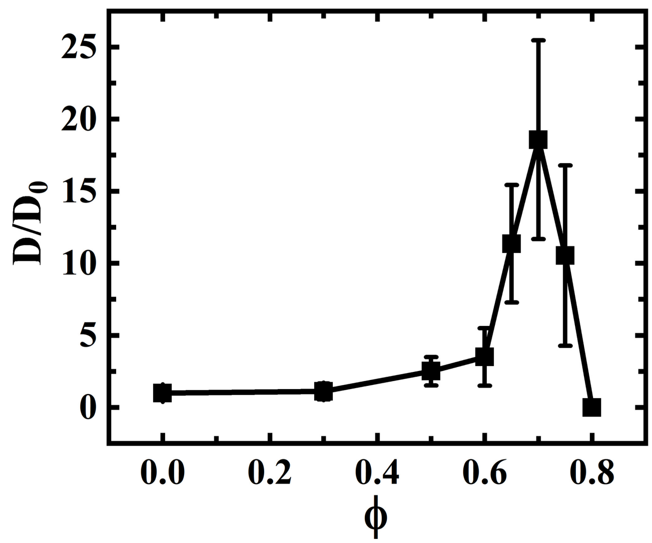

FIG. S6. Diffusion of chiral active Brownian particle. The relation between ϕ and D/D_0 for a CABP with $r = 3.76$ cm under square confinement with an outer boundary of 70 cm and an inner boundary of 14.5 cm. Error bars represent the standard deviation calculated over 3 independent measurements and are not visible when smaller than the symbol size.

accessible channel area identical to that of the annular geometry [Fig. S5]. The normalized diffusion coefficient D/D_0 still exhibits a pronounced nonmonotonic dependence on the obstacle area fraction ϕ, with a maximum occurring at the same intermediate density $\phi_c = 0.70$ as observed in the annular configuration [Fig. S6]. This demonstrates that the nonmonotonic diffusion enhancement is not specific to annular confinement, but instead reflects a generic mechanism arising from the competition between obstacle-induced motion collimation and migration suppression in reconfigurable disordered media.

SUPPLEMENTARY NOTE 4: DIFFUSION BEHAVIOR OF ACHIRAL PARTICLE

To further examine the role of chirality, additional control experiments were performed using achiral particles [Fig. S7]. The diffusion coefficient decreases monotonically with increasing the obstacle area fraction ϕ, suggesting that the nonmonotonic diffusion enhancement observed in this study is closely associated with particle chirality.

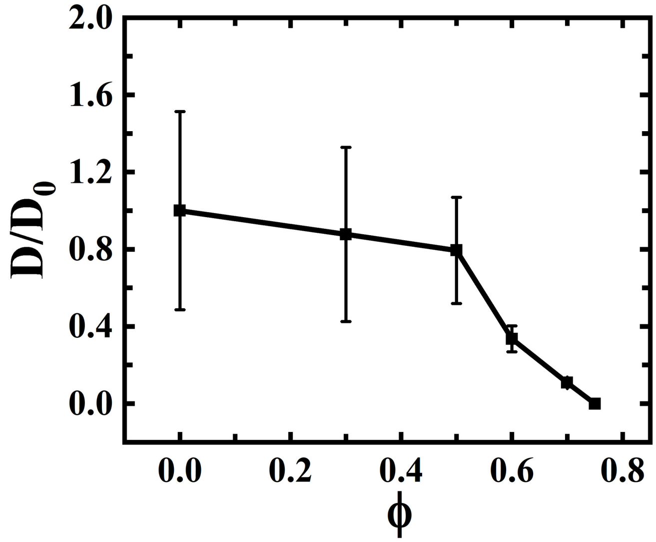

FIG. S7. Diffusion dynamics of achiral particle. Normalized diffusion coefficient of achiral particle as a function of obstacle area fraction. Error bars represent the standard deviation calculated over 3 independent measurements and are not visible when smaller than the symbol size.

SUPPLEMENTARY NOTE 5: DEFINITION OF R_c

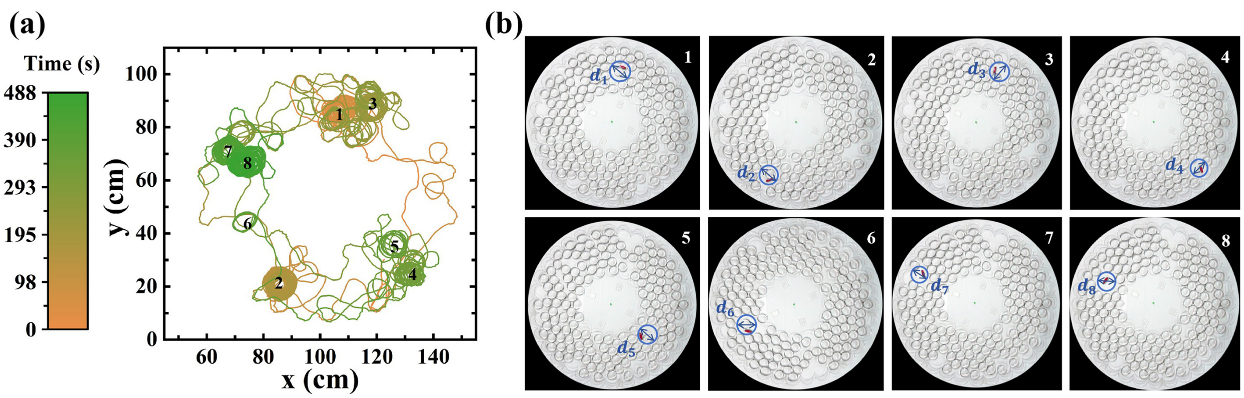

FIG. S8. Trajectory and trapped regions of a chiral active Brownian particle. (a) Trajectory of a CABP with orbital radius r = 3.76 cm at obstacle area fraction of $\phi = 0.6$. (b) Blue circles indicate eight identified trapped regions, with d_1, d_2,..., d_8 denoting their respective diameters.

A chiral active Brownian particle is classified as trapped if it remains confined within a circular region of radius R_c and its residence time exceeds that required for two complete free-space rotations. R_c is defined as the average diameter [Fig. S8(b)] of all identified trapped regions,

$$R_c = \frac{1}{n}\sum_{i=1}^{n} d_i, \tag{S1}$$

where n is the number of trapped regions and d_i is the diameter of the i-th trapped region.

SUPPLEMENTARY NOTE 6: TEMPORAL ROBUSTNESS OF TRAPPING CRITERION: REQUIRING THREE FULL ROTATIONS

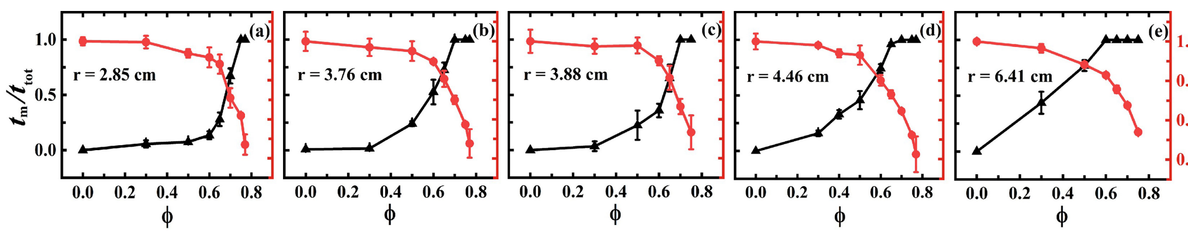

FIG. S9. Experimental results under the criterion of three full rotational cycles. (a)-(e) Normalized migration time (black triangles) and velocity (red circles) as functions of obstacle area fraction ϕ for CABPs with different orbital radii r. Error bars denote the standard deviation from 3–7 independent measurements and are not visible when smaller than the symbol size.

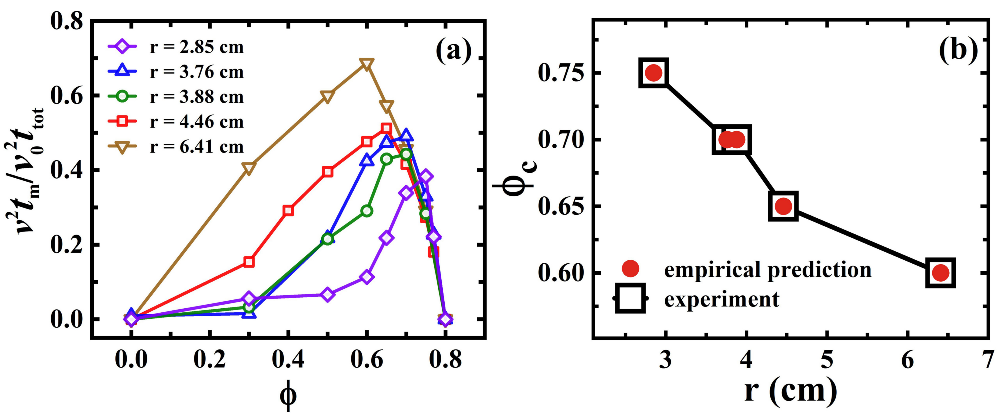

FIG. S10. Analysis under the three rotation trapping criterion. (a) $v^2 t_m/v_0^2 t_{tot}$ for different CABPs as functions of obstacle area fraction ϕ. (b) Critical area fraction ϕ_c corresponding to the peak of experimentally measured D/D_0 (black squares) and empirical prediction (red dots) for CABPs with different r.

To evaluate the robustness of the trapped-state definition, we apply another temporal criterion by increasing the minimum number of rotations within the localized region from two to three full cycles. As shown in Figs. S9 and S10, this modification yields trapping durations that are statistically indistinguishable from those obtained under the original two-cycle criterion [see Fig. 4 and Fig. 5(c) in the main text]. These findings confirm the validity and stability of the initial classification, indicating that the trapping definition is robust with respect to increased temporal stringency.

SUPPLEMENTARY NOTE 7: DEFORMATION AND CIRCULARITY OF THE OBSTACLES

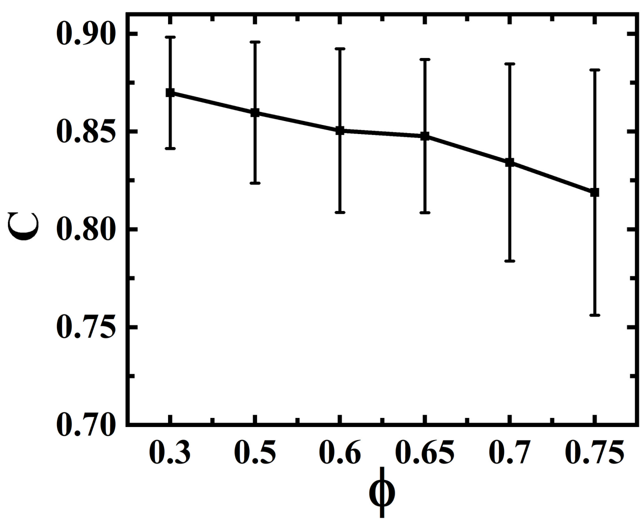

FIG. S11. Circularity of soft rings. Circularity $C = 4\pi S_r/L_P^2$ of the soft rings at different obstacle area fractions ϕ in the presence of a CABP with $r = 3.76$ cm. Error bars represent the standard deviation calculated over 3 independent measurements.

To provide a quantitative characterization of the deformation of the soft rings, the obstacle shapes and their circularity was evaluated, defined as $C = 4\pi S_r/L_P^2$, where S_r and L_P denote the area enclosed by a ring and its perimeter. For a perfect circle, $C = 1.0$. As shown in Fig. S11, the average circularity of the soft rings remains $C > 0.8$ across all obstacle area fractions ϕ explored in the experiments, indicating that the obstacles remain largely circular and that deformations under the present conditions are small and elastic.

The apparent non-circular shapes observed in the videos arise primarily from experimental and imaging factors rather than irreversible deformation. In particular, the imaging geometry, with the camera positioned above the center of the annular setup, may introduce slight visual distortions and shadow effects near the ring boundaries. In addition, transparent tape used at the attachment points of the soft rings can locally reduce curvature, leading to small deviations from perfect circularity.

SUPPLEMENTARY NOTE 8: DETERMINATION AND SENSITIVITY ANALYSIS OF THRESHOLD PARAMETER b

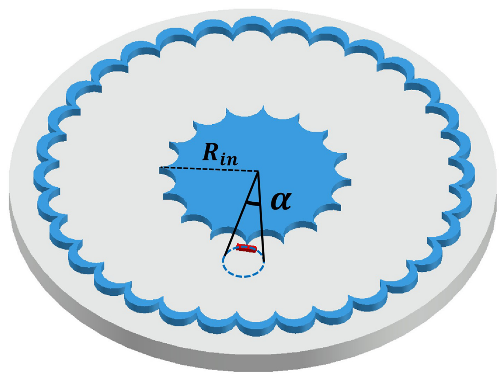

FIG. S12. Representative trajectory of a chiral active Brownian particle performing a complete circular orbit near the inner boundary of the annular channel. The particle is marked by a red rectangle, and the system boundaries are indicated by the blue shaded regions.

As illustrated in Fig. S12, the blue dashed circle represents the trajectory of a CABP undergoing rotational motion near the inner boundary. Upon completing a full rotation, the maximum azimuthal angular displacement along the annular channel is given by

$$\alpha = 2 \arcsin\left(\frac{r}{r + R_{in}}\right), \tag{S2}$$

where $R_{in} = 20$ cm denotes the radial distance from the system center to the inner boundary, and r is the orbital radius of the CABP. To quantify escape from localized confinement, the angular escape threshold b is defined as the minimum azimuthal displacement required for a CABP to be considered as having exited its initial region. Figure S13 shows the temporal evolution of the self-overlap function $Q(t)$ obtained using $b = 2\alpha = 4 \arcsin[r/(R_{in} + r)]$, which closely agrees with the results computed using $b = 1.5\alpha = 3 \arcsin[r/(R_{in} + r)]$ [see

Fig. 3 in the main text]. This consistency confirms that the statistical characterization is robust with respect to moderate variations in the threshold parameter.

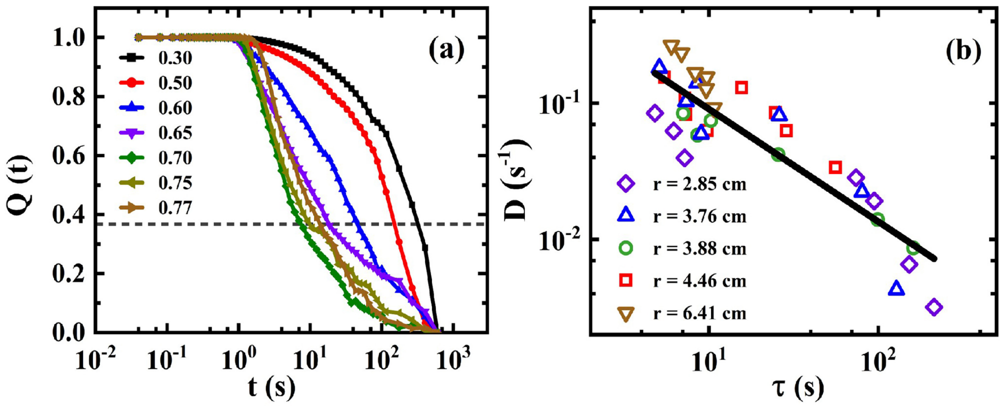

FIG. S13. Relaxation dynamics and scaling behavior. (a) Self-overlap function $Q(t)$ for a CABP with orbital radius $r = 3.76$ cm, calculated using an angular escape threshold $b = 4\arcsin[r/(R_{in} + r)]$. (b) Scaling relation between the effective diffusion coefficient D and relaxation time τ for CABPs with varying r and obstacle area fraction ϕ, confirming the robustness of the power-law behavior. The black solid line denotes the best fit, $D \propto \tau^{-0.82}$.

SUPPLEMENTARY NOTE 9: MEAN RADIAL COORDINATE AND TRANSLATIONAL DIFFUSION

As shown in Fig. S14(a), the mean radial coordinate of the five CABPs remains approximately constant over the explored range of obstacle area fraction ϕ, allowing radial fluctuations to be neglected and transport to be characterized by the angular diffusion coefficient. Accordingly, the effective diffusion coefficient adapted from the literature [1] is applied to the angular MSD and converted to a physical diffusivity through the mean radial coordinate, yielding the correct physical dimension and allowing direct comparison with the conventional translational diffusion coefficient.

The normalized two-dimensional translational diffusion coefficient D_t/D_t^0 was further independently measured at different ϕ [Fig. S14(b)]. Its dependence on ϕ closely matches that of the normalized angular diffusion coefficient D/D_0, including identical peak positions. This agreement confirms that the 2D effective diffusion framework captures the essential transport behavior in our system and justifies its application to the angular MSD analysis.

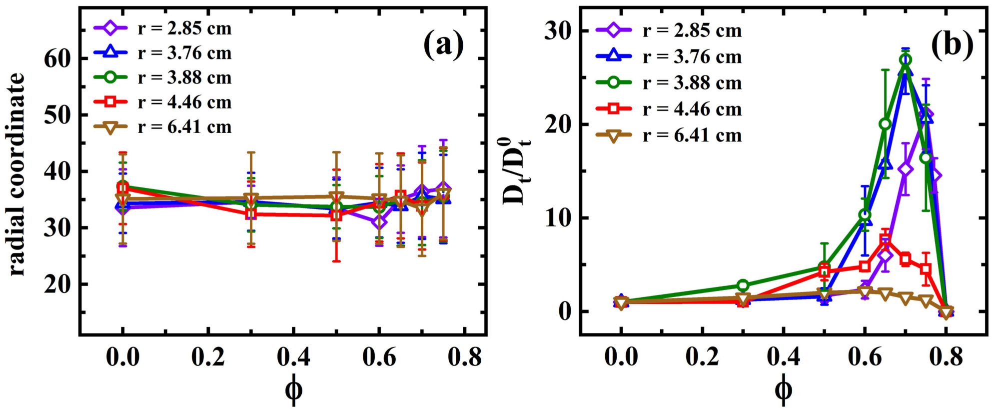

FIG. S14. Mean radial coordinate and translational diffusion of chiral active Brownian particles. (a) Mean radial coordinate of five CABPs as a function of obstacle area fraction ϕ. (b) Normalized translational diffusion coefficient D_t/D_t^0 of five CABPs versus ϕ. respectively. Error bars represent the standard deviation from 3–7 independent measurements and are not visible when smaller than the symbol size.

SUPPLEMENTARY NOTE 10: PREDICTION OF OPTIMAL OBSTACLE DENSITY ϕ_c FROM EMPIRICAL FITS

r (cm)	2.85	3.76	3.88	4.46	6.41
A_1	8×10^{-5}	0.001	0.001	0.01	0.15
b_1	12.5	10	10	6.67	3.125
y_2	1	1	1	1	1
A_2	2.0×10^{-4}	4.5×10^{-5}	4.6×10^{-4}	5.6×10^{-4}	3.6×10^{-3}
b_2	11	13	10	10	7

TABLE S1. Fitting parameters. A_1, b_1, y_2, A_2, and b_2 for CABPs with different radii r.

The empirical fitting was performed for all CABPs with different orbital radii, as shown in Fig. S15, and the corresponding fitting parameters vary with r [Table. S1]. The same functional form remains applicable across all cases. This extended analysis confirms that the empirical functional forms consistently capture the competition between migration enhancement and velocity suppression for all CABPs studied.

We have additionally overlaid the experimental diffusion data from Fig. 2(b) with the diffusion estimate constructed from the combined normalized rotational and translational

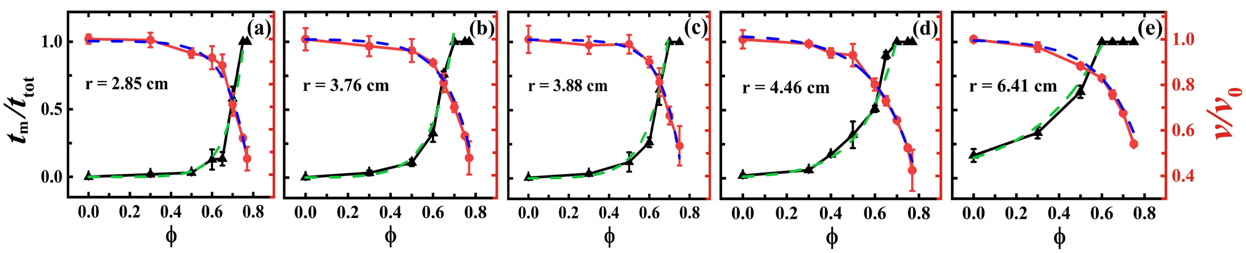

FIG. S15. Migration time and velocity. Normalized migration time (black samples) and velocity (red circles) of CABPs with (a) $r = 2.85$ cm, (b) $r = 3.76$ cm, (c) $r = 3.88$ cm, (d) $r = 4.46$ cm, and (e) $r = 6.41$ cm, as functions of ϕ. The dashed lines represent fits to the experimental data using empirical functions $t_m/t_{tot} = A_1 e^{b_1\phi}$ (green) and $v/v_0 = 1/(y_2 + A_2 e^{b_2\phi})$ (blue), respectively. Error bars denote the standard deviation from 3–7 independent measurements and are not visible when smaller than the symbol size.

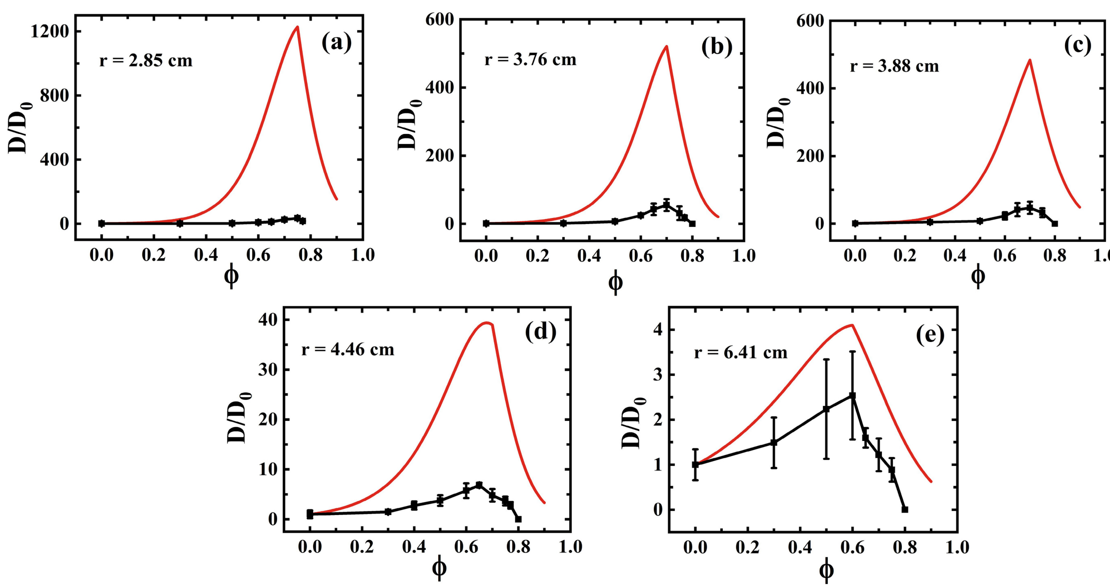

FIG. S16. Empirical prediction and experimental data. The empirical prediction (red line) and experimental data (black line) of the normalized diffusion coefficient for CABPs with different r, as functions of ϕ. The orbital radius (a) $r = 2.85$ cm, (b) $r = 3.76$ cm, (c) $r = 3.88$ cm, (d) $r = 4.46$ cm, and (e) $r = 6.41$ cm. respectively. Error bars denote the standard deviation from 3–7 independent measurements and are not visible when smaller than the symbol size.

friction coefficients, $\gamma_r/\gamma_r{}^0$ and $(\gamma_t{}^0/\gamma_t)^2$, as shown in Fig. S16. This comparison shows that the scaling framework successfully captures the nonmonotonic dependence on ϕ and correctly identifies the location ϕ_c of the diffusion maximum of CABPs in complex media, although quantitative deviations between the estimated and measured values remain.

We speculate that these quantitative deviations arise from the simplifying assumption that the influence of the obstacle background can be fully absorbed into effective friction coefficients. In practice, CABP-obstacle collisions may also generate additional stochastic contributions, analogous to noise, which are expected to be active and colored rather than equilibrium thermal noise. Moreover, such active and maybe environment-dependent noise are difficult to incorporate within a simple scaling description. In the present analysis, we therefore retain only the frictional effects and neglect these noise contributions. Importantly, this approximation does not affect the qualitative trends or the predicted location of optimal diffusion enhancement.

SUPPLEMENTARY NOTE 11: PERSISTENCE TIME AND PERSISTENCE LENGTH

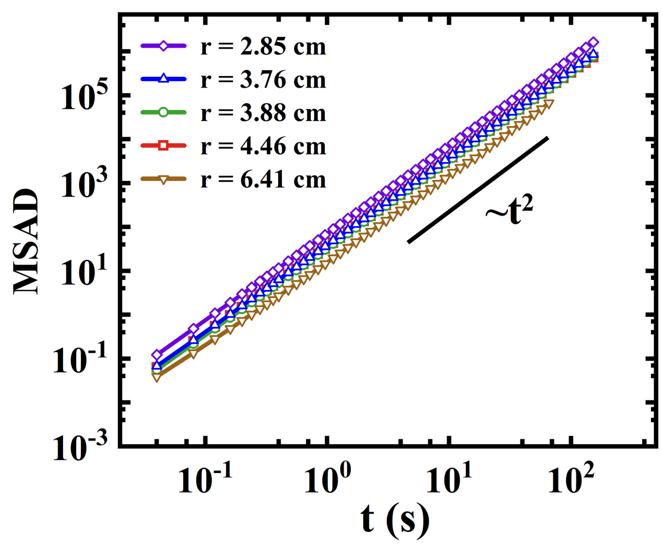

FIG. S17. Rotational diffusion of chiral active Brownian particles. The MSAD of five particles as a function of delay time t without soft-ring obstacles.

The persistence time and persistence length are explicitly calculated from the trajectories of CABPs in the obstacle-free environment using a standard approach as following. The effective rotational diffusion coefficient D_r is extracted from mean squared angular displacement (MSAD), MSAD= $\langle[\varphi(t_0 + t) - \varphi(t_0)]^2\rangle = \omega^2 t^2 + 2D_r t$ [Fig. S17], where $\varphi(t)$ denotes the orientation angle of the particle's major-axis [2]. The persistence time τ_r is then defined as $\tau_r = 1/D_r$ in two-dimensional system [3], and the corresponding persistence length $l = v_0\tau_r$, with v_0 being the average translational speed measured in obstacle-free space.

SUPPLEMENTARY REFERENCES

[1] Ebbens, S., Jones, R. A. L., Ryan, A. J., Golestanian, R. & Howse, J. R. Self-assembled autonomous runners and tumblers. *Phys. Rev. E* **82**, 015304 (2010).

[2] Wykes, M. S. D. *et al.* Dynamic self-assembly of microscale rotors and swimmers. *Soft Matter* **12**, 4584–4589 (2016).

[3] Caprini, L., Löwen, H. & Marconi, U. M. B. Chiral active matter in external potentials. *Soft Matter* **19**, 6234–6246 (2023).